3D-CFD and experimental comparison of two-phase flow generation in a micro T-junction

S. Arias[a] and A. Montlaur [b]
Universitat Politècnica de Catalunya - BarcelonaTech,

Castelldefels, Barcelona (Spain), 08860

This paper presents a 3D numerical study of the bubble generation process in a T-junction, performed with the commercial Computational Fluid Dynamics solver ANSYS Fluent v15.0.7. Numerical results on bubble generation frequency, bubble velocity, volume void fraction, bubble volume, and characteristics bubble lengths are compared with experimental data. Additionally, a new simple fitting for the bubble generation frequency, based upon previously reported experimental works, is proposed here.

[a] Aerospace Lecturer, Escola d'Enginyeria de Telecomunicació i Aeroespacial de Castelldefels, Universitat Politècnica de Catalunya, c/ Esteve Terradas 5, 08860 Castelldefels, Barcelona (Spain).

[b] Associate Professor, Escola d'Enginyeria de Telecomunicació i Aeroespacial de Castelldefels, Laboratori de Càlcul Numèric (www-lacan.upc.edu), Universitat Politècnica de Catalunya, c/ Esteve Terradas 5, 08860 Castelldefels, Barcelona (Spain),

Nomenclature

A = capillary cross-section area

a_0 = initial slope of the linear regime

Bo = Bond number

Ca = capillary number

C_0 = void fraction distribution coefficient

f = bubble generation frequency

f_{sat} = saturation frequency

g = acceleration of gravity

L = length

Q = volumetric flow rate

Re = Reynold number

U = velocity

V = volume

We = Weber number

α = volume average void fraction

β = volumetric gas quality

Δt = time step

ϵ = relative error

ϕ_B = bubble equivalent diameter

ϕ_c = capillary internal diameter

μ = dynamic viscosity

ρ = density

σ = surface tension

B = bubble

G = gas

L = liquid

UC = unit cell

I. Introduction

Capillary gas-liquid two-phase flows occur in increasingly more modern applications in space-based systems. This is mainly due to the fact that two-phase systems present an improvement in performances and efficiency, as well as significant reductions in weight, with respect to single-phase systems. Some remarkable examples in different aerospace fields can be found for example in space bioreactors, chemical contactors, life support systems for human exploration and development of space (HEDS), thermal management systems and propulsion systems. A full understanding of the behaviour of gas-liquid interface and flow characteristics in gravity reduced environments is thus a major necessity for the development of these technologies. Different methods have been developed to produce controlled two-phase flows in microgravity conditions. In this paper, we focus on the analysis of a micro T-junction in which bubbles are generated and dispersed into a continuous liquid in a very regular way and with small dispersion in bubble size.

Numerous experimental studies have been made on the generation of bubbles and droplets in T-junction bubble generators as the ones performed in [1, 2]. In the recent past, different Computational Fluid Dynamics (CFD) methods have also been used in order to study similar devices. A commercial CFD package was used by Qian & Lawal [3] to simulate the squeezing regime during the bubble formation in a T-junction microchannel, focusing on studying the effects of pressure, surface tension and shear stress action on the gas thread. Kashid et al. [4] discussed CFD modelling aspects of internal circulation and slug flow generation. The slug flow formation in a 120° Y-junction was simulated and velocity profiles inside the slug were obtained. A numerical investigation by means of a phase-field model of the breakup dynamics of streams of immiscible fluids in a microfluidic T-junction was carried out by De Menech et al. [5], where three regimes of formation of droplets (squeezing, dripping and jetting) were identified and analysed.

More recently, Arias et al. [6] presented a fluid dynamics numerical study on the formation of mini-bubbles (bubbles with a diameter of the order of 10^{-3} m) in a 2D T-junction, and results on the behaviour of bubble velocity, volume void fraction, bubble generation frequency and characteristic lengths were obtained and compared to experimental data. Also using a two-dimensional numerical model with Volume of Fluid method (VOF), the phenomena of alternating droplet formation, with

applications such as nanoparticle synthesis, hydrogel bead generation, and cell transplantation in biomedical therapy, was studied by Ngo et al. [7]. Malekzadeh & Roohi [8] focused in the two-dimensional bubble formation process by analysing in detail the effects of three main parameters, that are: the capillary number, the contact angle and the gas-liquid flow rate ratio. As for 3D simulations, droplet formation in T-junction microchannels was studied using the Lattice Boltzmann method by Shi et al. [9] and simulations in heat exchangers using the VOF method were performed by Ben Saad et al. [10].

The paper presented here is a continuation of the study by Arias et al. [6], completing it and extending it to 3D. Some parameters are now studied in more depth, such as the bubble generation frequency, a new fit for frequency being used here, and new values of interest are presented, such as the bubble volume, the bubble equivalent diameter and the unit cell length. Section II presents the T-junction problem statement. Section III summarises the methodology used in the experimental study, following the one used in Arias et al. [6], as well as the hypotheses used in the numerical simulations and their validations. Section IV exposes the results of the numerical simulations and compares them to the experimental ones. Finally some conclusions are drawn in section V.

II. Problem statement

This study aims to simulate a bubble generator in which liquid and gas are injected at perpendicular directions into a 1 mm internal diameter capillary T-junction with a total length of 10 mm, see figure 1. In order to compare numerical simulations with realistic results, CFD simulations have been carried out following the experimental conditions as much as possible. The fluids used in experiments and CFD simulations are air and water, both of them considered incompressible and isothermal, at a room temperature of 25°C. Standard physical values at that given temperature are assumed for viscosity ($\mu_G = 10^{-5}$ Pa.s and $\mu_L = 10^{-3}$ Pa.s for air and water, respectively), density ($\rho_G = 1.225$ kg/m^3 and $\rho_L = 10^3$ kg/m^3 for air and water, respectively) and surface tension at the gas-liquid interface ($\sigma = 0.072$ N/m).

The experimental setup used in this study has been reported in previous works by Arias et al. [11, 12]. Its particularity is that the gas and liquid volumetric flow rates can be controlled in a very accurate way. Note that, in the whole study results are presented as a function of the superficial

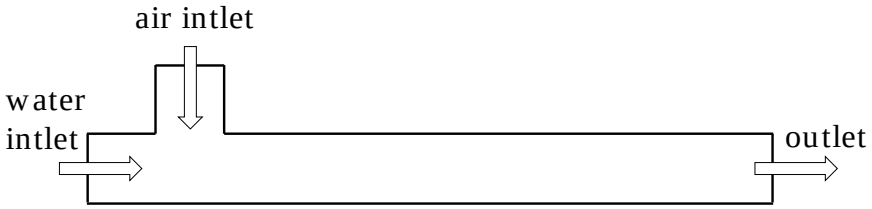

Fig. 1 Sketch of T-junction

velocities defined as $U_{SG} = Q_G/A$ and $U_{SL} = Q_L/A$, where U_{SG} and U_{SL} are the gas and liquid superficial velocities, Q_G and Q_L the gas and liquid volumetric flow rates, and A the capillary cross-section area.

The gas superficial velocities used in the experiments range from 0.062 to 0.473 m/s, whereas three values (0.106, 0.318 and 0.531 m/s) are used for the liquid superficial velocity. A total of 23 experiments are compared with the results obtained in the numerical simulations. Although the core of this work is the simulation of 3D two-phase flows, 16 new experiments widen and complement the knowledge provided by the 7 experiments previously presented in Arias et al. [6]. Additionally, three more simulations were conducted at a very low gas flow rate ($U_{SG} = 0.025$ m/s) for each liquid superficial velocity (note that no experiment had been conducted for this U_{SG} value).

The dimensionless Bond number (Bo) represents the balance between gravitational and surface tension forces. Bo is commonly defined as $(\rho_L - \rho_G)g\phi_c^2/\sigma$, where ρ_L and ρ_G are the liquid and gas densities, g the gravitational acceleration, ϕ_c the capillary internal diameter and σ the surface tension at the gas-liquid interface. ρ_L is usually much larger than ρ_G ($\Delta\rho \approx \rho_L$), which leads to the next simplified definition of the Bond number: $B_o = \rho_L g\phi_c^2/\sigma$. Following this last definition, $Bo = 0.139$ in this study. As a consequence, gravity plays a smaller role than the surface tension in the bubble generation process, and the formation and detachment of bubbles is mainly dominated by the competition between the capillary and the liquid drag forces, which can be evaluated by the Weber number. Suo & Griffith [13] developed a criterion based on the Bond number that determines that gravitational effects become negligible with respect to capillary effects when $Bo < 0.29$, resulting in the irrelevance of the channel orientation. Therefore, the present analysis can be considered gravity independent and assuming $g = 0$ m/s^2 becomes a valid approach for the numerical simulations.

The gas Weber number can be defined as $We_G = \rho_G \phi_c {U_G}^2/\sigma$, where U_G is the gas velocity, also commonly referred as bubble velocity. According to Rezkallah [14], when the criterion $We_G \lesssim 2$ is accomplished, capillary forces overcome inertial forces, and the bubble formation is controlled by the surface tension. Only bubble and slug flow regimes are expected to be observed in these circumstances. In our experiments, 0.159 m/s $\leq U_G \leq$ 1.143 m/s (more information about the bubble velocity can be found in section IV B), which leads to $4.3\times10^{-4} \leq We_G \leq 2.2\times10^{-2}$, corresponding to the surface tension controlled region. The liquid Weber number ($We_{SL} = \rho_L \phi_c {U_{SL}}^2/\sigma$) ranges from 0.16 to 3.92.

The average mixture superficial velocity Reynolds number can be defined as $Re_M = \rho_L \phi_c U_M/\mu_L$, where U_M is the sum of the gas and liquid superficial velocities. In the experiments, 0.167 m/s $\leq U_M \leq$ 1 m/s, which leads to $167 \leq Re_M \leq 1000$. The liquid superficial velocity Reynolds number ($Re_{SL} = \rho_L \phi_c U_{SL}/\mu_L$), ranges from 106 to 530. These values of Re_M and Re_{SL} correspond to flows in laminar conditions.

Finally, the capillary number $Ca = We/Re$ is used to compare viscous forces and surface tension effects at the interface. The corresponding range of the capillary number, based on the liquid superficial velocity, is $1.5 \times 10^{-3} \leq Ca_{SL} \leq 7.4 \times 10^{-3}$.

Having used the same fluid physical properties and gas and liquid superficial velocities in experiments and simulations, the bubble generation behaviour in numerical simulations is expected to be similar to the experimental one.

III. Methodology

A. Experiments

Experiments were performed at constant liquid superficial velocity while increasing the gas superficial velocity. For each pair of velocities U_{SG}-U_{SL}, images were taken with a high-speed camera at 4000 f.p.s. once the flow stabilised and the generation of bubbles was regular and periodic. Images of the two-phase flows were classified into bubble or slug flow regimes, according to the Dukler's criterion (see section IV). Bubble generation frequency was measured by counting the total number of bubbles over a long period of time, whereas the bubble velocity was measured directly over the calibrated images, by taking into account the displacement of the foremost part of a single bubble.

The unit cell length was also measured over the calibrated images. It was measured, both in the experiments and in the numerical simulations, as the distance between the most forward points of two consecutive bubbles.

B. Numerical simulations

1. Flow solver

All numerical simulations were carried out using a commercial CFD solver, ANSYS Fluent v15.0.7. Note that this CFD solver is different from the numerical code JADIM used in [6]. The VOF method was used to model the two immiscible fluids by solving a single set of momentum equations and tracking the volume fraction of each fluid throughout the domain. In each control volume, the volume fractions of both phases sum to unity.

The tracking of the interface between the phases is accomplished by the solution of a continuity equation for the volume fraction of one of the phases [15]. For the q^{th} phase, this equation has the following form:

$$\frac{1}{\rho_{\text{q}}}\left[\frac{\partial}{\partial t}(\alpha_q \rho_q) + \nabla\cdot(\alpha_q \rho_q \mathbf{v_q}) = \sum_{p=1}^{n}(\dot{m}_{\text{pq}} - \dot{m}_{\text{qp}})\right] \tag{1}$$

where ρ_{q}, α_q and $\mathbf{v_q}$ are the density, volume void fraction and velocity of phase q, $\dot{m}_{\text{pq}}$ is the mass transfer from phase p to phase q and $\dot{m}_{\text{qp}}$ is the mass transfer from phase q to phase p. The volume fraction equation is not solved for the primary phase; the primary-phase volume fraction is computed based on the following constraint: $\sum_{q=1}^{n} \alpha_q = 1$.

The fields for variables and properties are shared by the phases and represent volume-averaged values, as long as the volume fraction of each of the phases is known at each location. Thus the variables and properties in any given cell are either purely representative of one of the phases, or representative of a mixture of the phases, depending on the volume fraction values. That is, if the water volume fraction in the cell is denoted as a_w, then three conditions are possible. If $a_w = 0$, the cell is empty of water, if $a_w = 1$, the cell is full of water, and if $0 < a_w < 1$, the cell contains the interface between water and air [15]. Based on the local value of a_w, the appropriate properties and variables are assigned to each control volume within the domain.

An explicit formulation is used for the VOF model, with a Courant number of 0.25, and the PRESTO! (PREssure STaggering Option) scheme is used for pressure interpolation. This scheme uses the discrete continuity balance for a staggered control volume about the face to compute the staggered pressure. This procedure is similar in spirit to the staggered-grid schemes used with structured meshes [15]. For the volume fraction spatial discretisation scheme, the geometric reconstruction scheme is used, which represents the interface between fluids using a piecewise-linear approach. In Fluent this scheme is the most accurate and is applicable for general unstructured meshes. The geometric reconstruction scheme is generalised for unstructured meshes from the work of Youngs [16]. Finally, a second-order upwind scheme is used for spatial discretisation.

The VOF method also includes the effects of surface tension along the interface between each pair of phases. The surface tension model in Fluent is the continuum surface force model proposed by Brackbill et al. [17]. With this model, the addition of surface tension to the VOF calculation results in a source term in the momentum equation. As commented in section II, a surface tension of 0.072 N/m is applied.

The following boundary conditions were set for the numerical simulations. All walls are treated as no-slip smooth walls. A wall adhesion angle in conjunction with the surface tension model is also applied in the VOF model [17]. Rather than imposing this boundary condition at the wall itself, the contact angle that the fluid is assumed to make with the wall is used to adjust the surface normal in cells near the wall [15]. This so-called dynamic boundary condition results in the adjustment of the curvature of the surface near the wall. The contact angle is the angle between the wall and the tangent to the interface at the wall. A contact angle of 0° was set up as wall adhesion (hydrophilic condition) on the horizontal walls, and of 25° on the vertical walls, based on experimental data from Arias et al. [6], see Section III B 3 for more details on this.

Water and air inlets are considered as velocity inlets, with the corresponding fluid velocity in each case of study, namely U_{SG} and U_{SL}. At the water inlet, the fraction of water is considered as 1 and at the air inlet, the fraction of air is the one set to 1. The outlet of the T-junction is set up as a pressure outlet.

An operating pressure of 101325 Pa is set up at a point close to the air inlet, that is, at a point

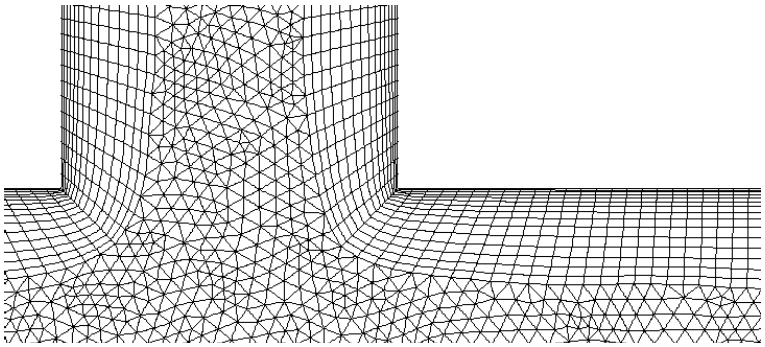

Fig. 2 Close-up view of the hybrid mesh in the pinch-off zone

where there will always be only air. Finally the gravity value is set to 0, as explained in Section II.

2. Mesh

The computational mesh was composed of 413000 elements. An inflation mesh comprising 15 layers was used along all the walls, with a first layer height of 0.005 mm. A body sizing of 0.045 mm was used in all the domain. The resulting mesh is a mix of hexahedral (close to the walls) and tetrahedral (in the core of the domain) elements, as it can be seen in Figure 2. The hex dominant option has been chosen, resulting in a fewer number of elements than if mainly tetrahedral elements had been considered. Mesh independence is presented in section III B 3.

A first-order implicit scheme is used for the transient formulation. Time step independence is also presented in section III B 3. In order to obtain a converged solution, the calculation was always continued until at least 7 or 8 bubbles of air were generated.

3. CFD validation

The mesh convergence is first checked. Three meshes are considered: a coarse one (220000 elements), a second one (413000 elements) obtained by multiplying the body sizing and first layer height of the boundary layer by 0.75, and a third one (879000 elements), obtained by multiplying again the mesh dimensions by 0.75. Three independent parameters of study are used: the bubble frequency (f), velocity (U_G) and volume (V_B). Absolute values and percentages of error with respect to the finest mesh are shown in table 1, for $U_{SL} = 0.318$ m/s and $U_{SG} = 0.242$ m/s.

Table 1 Study of mesh convergence for three meshes and three independent parameters

number of elements	f [1/s]	ϵ_f [%]	U_G [m/s]	ϵ_{U_G} [%]	V_B [$\times 10^{-10}$m^3]	ϵ_{V_B} [%]
220000	266.7	14.7	0.649	7.1	7.31	8.1
413000	238.1	2.4	0.625	3.1	7.82	1.6
879000	232.6	–	0.606	–	7.95	–

Table 2 Study of time convergence for three Δt and three independent parameters

Δt [s]	f [1/s]	ϵ_f [%]	U_G [m/s]	ϵ_{U_G} [%]	V_B [$\times 10^{-10}$m^3]	ϵ_{V_B} [%]
10×10^{-6}	243.9	3.5	0.633	1.9	8.04	5.0
5×10^{-6}	238.1	1.1	0.625	0.6	7.82	2.1
2.5×10^{-6}	235.6	–	0.621	–	7.66	–

These results show that for the 413000-element mesh, errors due to the mesh remain within a relatively small margin ($\leq 3.1\%$); this is thus the mesh that has been chosen for the numerical study.

Next, the influence of the time step has been studied considering the chosen mesh of 413000 elements. Three values of Δt are considered: 2.5×10^{-6}, 5×10^{-6} and 10×10^{-6} s. Again absolute values of bubble frequency, velocity and volume are shown in table 2, as well as the percentages of error with respect to the smallest Δt, for $U_{SL} = 0.318$ m/s and $U_{SG} = 0.242$ m/s.

Table 2 shows that the three values of Δt lead to similar values (all errors $\leq 5.0\%$), smaller for the value of $\Delta t = 5 \times 10^{-6}$ s ($\leq 2.1\%$) than for the value $\Delta t = 10 \times 10^{-6}$ s. Therefore, the middle value, $\Delta t = 5 \times 10^{-6}$ s, has been chosen for the rest of the CFD study.

In order to further validate the chosen mesh size and Δt value, both mesh and time convergence tests were repeated at $U_{SL} = 0.531$ m/s and $U_{SG} = 0.469$ m/s, which are the highest liquid and gas velocities in the study. Results showed errors of less than 3% between the mesh of 879000 and 413000 elements, and of less than 1% between $\Delta t = 2.5 \times 10^{-6}$ s and $\Delta t = 5 \times 10^{-6}$ s, confirming the adequacy of the chosen mesh and Δt.

Another critical parameter to validate is the contact angle boundary condition on the vertical wall. As commented in Section III B 1, a constant value of 25° is imposed on the vertical capil-

Table 3 Study of the influence of the contact angle boundary condition on three independent parameters

Contact angle	f [1/s]	ϵ_f [%]	U_G [m/s]	ϵ_{U_G} [%]	V_B [$\times 10^{-10}$m^3]	ϵ_{V_B} [%]
0°	253.2	26.6	0.621	1.3	7.40	−22.2
25°	238.1	19.1	0.625	1.9	7.82	−17.7
45°	214.1	7.1	0.622	1.4	8.79	− 7.5
60°	195.3	−2.3	0.617	0.6	9.33	− 1.8
90°	182.8	−8.6	0.614	0.1	9.84	3.6
Exp values	200.0	–	0.613	–	9.50	–

lary, based on experimental data from Arias et al. [6]. Nevertheless, several studies emphasise the complexity of the mathematical paradox that supposes a contact line moving along a no-slip solid surface, which is the case on the vertical wall. Of the three forces acting on the fluid (inertial, viscous, and surface tension, assuming gravity is negligible), theoretical studies suggest that the viscous dissipation becomes very strong near a moving contact line [18]. It then leads to a curvature of the interface that varies sharply near the contact line, which can cause the contact angle to differ significantly from the measured interface angle, even at short distances away from the contact line [19]. Given the complexity of this phenomenon, a detailed study of the dynamic contact angle is out of the scope of the study proposed here, and a constant value is therefore imposed on the vertical wall.

In order to validate the experimental value of 25°, different values are tested between 0° and 90°, and the influence on the bubble frequency, velocity and volume is studied and presented in Table 3, for $U_{SL} = 0.318$ m/s and $U_{SG} = 0.242$ m/s. Table 3 shows that the contact angle highly influences the numerical value of the bubble frequency, velocity and volume. CFD results get closer to the experimental ones for a contact angle between 45° and 60° for the bubble frequency, and for a value between 60° and 90° for the bubble volume, whereas the error of the bubble velocity is more or less constant and remains within the mesh error margin. Therefore, no single value of the contact angle can provide simultaneously close-to-experimental results for the bubble frequency, velocity and volume, not even for a single pair $U_{SL} - U_{SG}$.

Figure 3 now shows views of the bubble generation for the CFD simulations, for contact angles of 25°, 45° and 60°, and compares them to the experimental one. The moment just before the detachment of the bubble is studied. Contrary to the results from Table 3, it can be seen that for angles bigger than 25°, the detachment mechanism differs from the one observed in the experiment, and more significantly as the contact angle increases. The contact line reaches lower positions on the vertical wall for larger values of the contact angle, and consequently the pinch-off region moves downstream. From an experimental point of view, this displacement occurs when the liquid velocity or its viscosity increases, because the liquid shear force becomes dominant over the effect of the buildup of the pressure immediately upstream the bubble [20]. According to Oishi *et al.* [21], this effect starts to take place when the capillary number (C_{SL}) is greater than 5.8×10^{-3}. The experimental picture shown in figure 3 corresponds to a value $C_{SL} = 4.4 \times 10^{-3}$, in which regime the liquid shear force should not be strong enough to move downstream the pinch-off region as much as it is observed in the 60° numerical simulation. Therefore, this value of contact angle clearly contradicts experimental evidences, even though it provides close-to-experimental numerical results for the bubble frequency and volume. The best resemblance with experimental pinch-off is thus obtained for a contact angle of 25° in the numerical simulation, which is also confirmed by comparing the position of the contact line in the vertical capillary. For these reasons, and despite the numerical errors in the bubble frequency and volume observed for this value, a contact angle of 25° is chosen in the rest of the study.

4. CFD metrics

Figure 4 shows an example of data obtained as a post-process of the CFD simulations. It shows the propagation of the bubble, through the fraction of air at two cross-sections of the domain located at 7 and 8 mm from the beginning of the tube, as a function of time. This allows to calculate the bubble frequency f, as the inverse of the time T_f between two bubbles at the cross-section, and its velocity U_G, as the distance between two cross-sections (here 7 and 8 mm) divided by the time T_S needed for the bubble to travel this distance. Its volume V_B is also calculated from this figure, integrating the total fraction of air of a bubble over time A_B and multiplying by its velocity and by

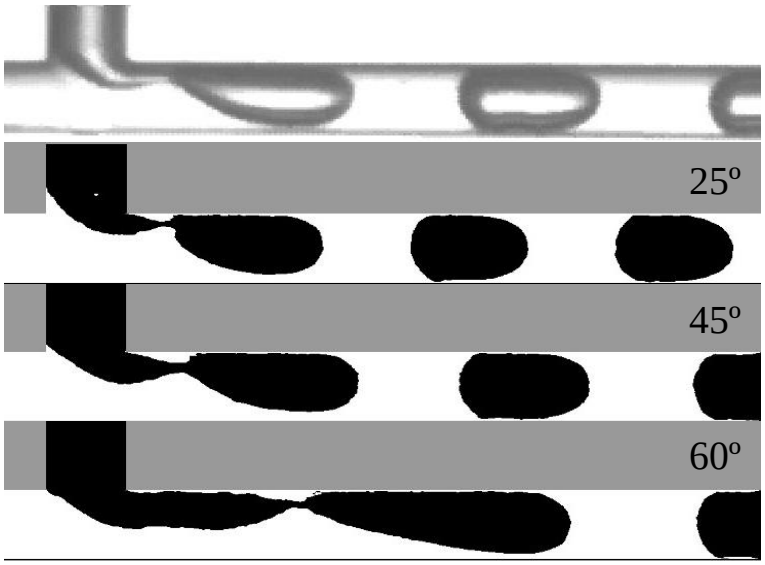

Fig. 3 Bubble generation at the moment just before detachment for contact angles of $25°$**,** $45°$**,** $60°$ **and the experimental one.** $U_{SL} = 0.318$ **m/s and** $U_{SG} = 0.242$ **m/s. The contact angle is indicated in the upper right corner**

the area of a 1 mm diameter circle. Since, this method could introduce some uncertainties related to U_G, the bubble volume was also computed defining the bubble interface at a given instant and integrating numerically the volume inside. This method was applied to three conveniently chosen U_{SL}-U_{SG} pairs (0.106-0.344, 0.318-0.242 and 0.531-0.068 m/s). The relative error was found to be smaller than 1.95% in all cases and the first method to compute V_B prevailed due to its simplicity.

Finally, the volume average void fraction, α, was estimated for both the experiments and the CFD simulations with the expression:

$$\alpha = \frac{U_{SG}}{U_G} \tag{2}$$

Note that defined in this way, the void fraction differs from the volumetric gas quality, β, which is defined as the ratio between the gas and the total volume flow rates: $\beta = Q_G/(Q_G + Q_L)$.

For this study, all simulations have been performed on a laptop computer, with 8.00GB of RAM and an Intel $i7-4500U$ @1.80GHz quad core CPU. It takes around 24 hours to simulate 30ms, that is, the fastest simulations were finished within a day whereas the slowest ones took up to 2 or 3 days.

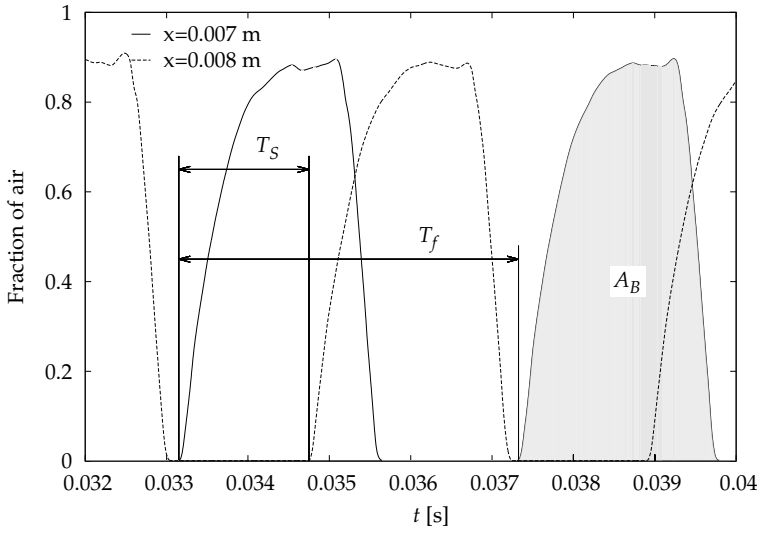

Fig. 4 Example of CFD post-processed results from the graph of fraction of air as a function of time, for $U_{SL} = 0.318$ m/s and $U_{SG} = 0.242$ m/s

IV. Results and discussion

A set of 26 new 3D numerical simulations are compared with a set of 23 experiments. 16 of these experiments are a novelty with respect to [6], as explained in section II. It can be seen that numerical simulations satisfactorily reproduce trains of bubbles as the ones obtained in experiments, see figures 5-7. Note that, as it will be detailed later, the bubble frequency is higher in the CFD simulation than in the experiments. Thus the choice has been made to show the trains of bubbles of figures 5-7 at the same stage of formation, which does not correspond to the same times.

In contrast with the study provided by Arias et al. [6], here no artificial pinch-off mechanism has been used in numerical simulations to detach bubbles. Bubbles were generated, both in experiments and numerical simulations, with high regularity and small size dispersion. Such periodicity allows to use the concept of unit cell, according to which the flow can be decomposed in duplicated units formed by a single bubble and a slug of liquid. The unit cell is mainly characterised by its length (see section IV C), which can be estimated as the distance between the tips of two consecutive bubbles.

Two types of flow patterns, the bubble and the slug flow regimes, were obtained in the simulations and in the experiments (accordingly to the criterion $We_G \lesssim 2$ explained in section II). As expected, no stratified, churn or annular flows were found for these values of gas and liquid superficial velocities neither in experiments nor in numerical simulations [13, 14, 22]. Both kinds

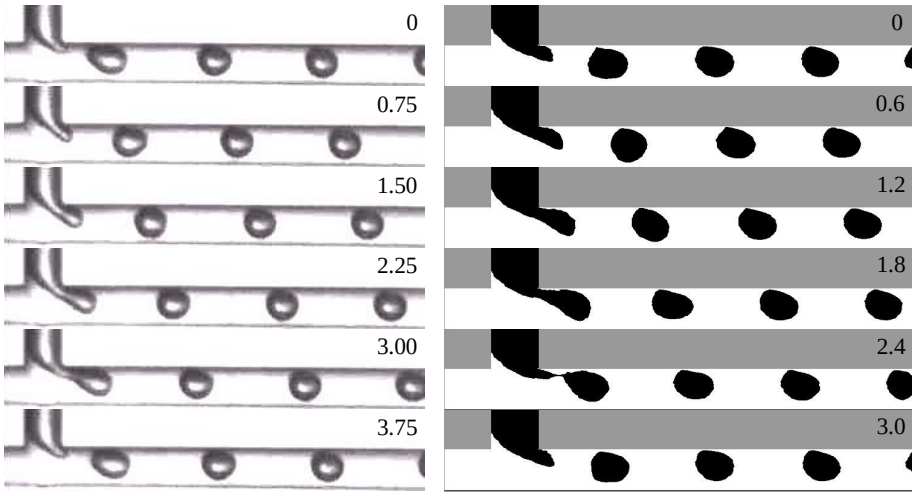

Fig. 5 Bubble flow in (*left*) experiments and (*right*) numerical simulations. $U_{SL} = 0.531$ **m/s and** $U_{SG} = 0.110$ **m/s. Time (ms) is indicated in the upper right corner**

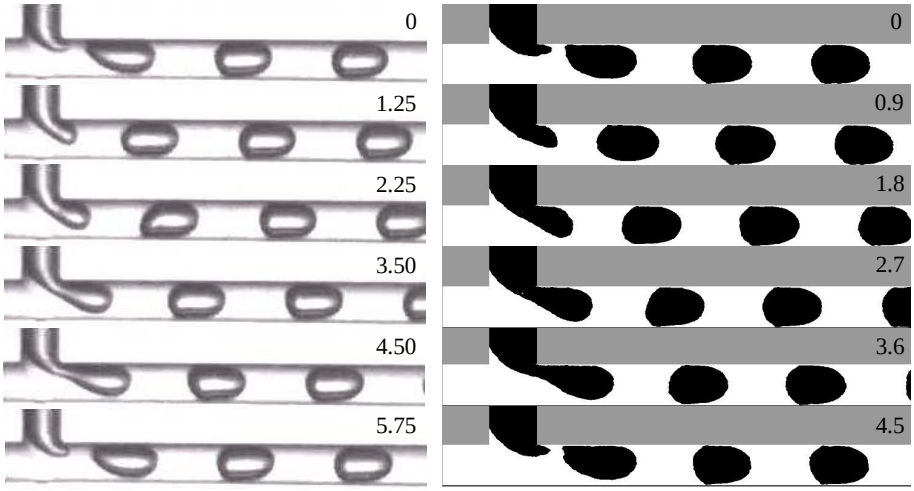

Fig. 6 Slug flow in (*left*) experiments and (*right*) numerical simulations. $U_{SL} = 0.318$ **m/s and** $U_{SG} = 0.182$ **m/s. Time (ms) is indicated in the upper right corner**

of flow patterns analysed here correspond to intermittent flows, in which the gas phase is dispersed into the liquid phase. Flows were classified into bubble or slug flow regime according to the Dukler's criterion [23], which defines the transition between the bubble and the slug flow regime as the moment when the bubble, assuming that it were spherical, reaches a diameter equal to the capillary diameter. Figs. 5 to 7 illustrate the generation of three bubbles with different sizes. Each figure shows the formation of a single bubble for different gas and liquid superficial velocities, as well as a train of similar bubbles. Fig. 5 corresponds to the formation of a bubble belonging to the bubble

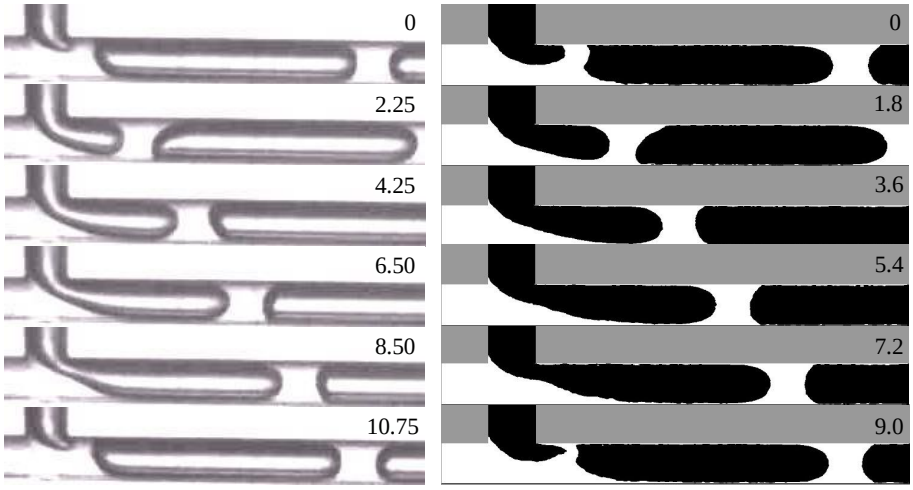

Fig. 7 Slug flow close to the slug-churn transition in (*left*) experiments and (*right*) numerical simulations. $U_{SL} = 0.106$ m/s and $U_{SG} = 0.471$ m/s. Time (ms) is indicated in the upper right corner

flow regime, its diameter being smaller than the capillary diameter. In this figure, bubbles are not exactly spherical. This is a consequence of the liquid drag and shear forces, which noticeably deform bubbles longitudinally. Figs. 6 and 7 show two examples of slug flow regime, the former being known as short Taylor bubble and the latter as middle Taylor bubble [24]. Bubbles from the slug flow regime are characterised by a bullet-shaped body, rounded at the front part and mainly flattened at the rear of it.

In every case, bubbles have an elongated rear part just after the detachment, this elongated shape being a remnant of the squeezed gas thread that was connecting the new bubble with the single-phase gas. From that moment, the effect of the surface tension tries to minimise the total surface of the bubble, which results in the vibration of the bubble surface until it stabilises. It can be seen that numerical simulations correctly reproduce the elasticity and fluctuation of the gas-liquid interface during the bubble detachment stage described here, but that the formation of bubbles was faster in the numerical simulations than in the experiments. This was expected from the contact angle study in Section III B 3, and the following sections will make further reference to this fact.

Next sections focus in a more exhaustive validation and comparison of numerical simulations with experimental data. Several parameters are selected to perform such a validation: bubble generation frequency, bubble velocity, volumetric void fraction, bubble equivalent diameter and

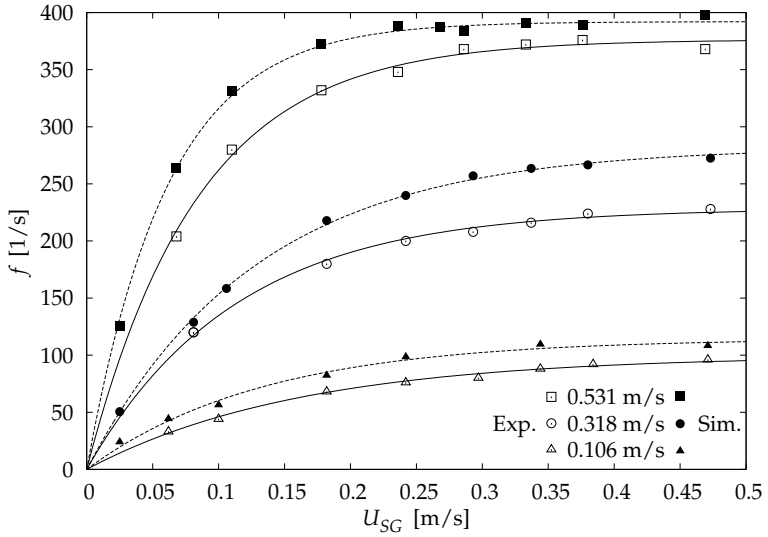

Fig. 8 Bubble frequency as a function of the superficial gas velocity for three different superficial liquid velocities. *Empty symbols*: experimental data, *solid symbols*: numerical data. *Solid lines*: fitting of the experimental data by using Eq. 3, *dashed lines*: fitting of the numerical data by using Eq. 3

unit cell length.

A. Bubble generation frequency

Figure 8 shows the evolution of the bubble generation frequency when increasing the superficial gas velocity. Data corresponding to three different liquid superficial velocities has been plotted for both experiments and numerical simulations. Although the same values of U_{SG} and U_{SL} from experiments were usually used in numerical simulations, some new values of U_{SG} were also simulated in order to enrich the knowledge about the behaviour of bubble generation frequency. This is the case of the three points at $U_{SG} = 0.025$ m/s, which are not present in the experimental data.

According to Arias et al. [11], at very low gas flow rate f follows a close-to-linear tendency that progressively curves when increasing U_{SG} until reaching a saturation value f_{sat}, which remains constant thereafter. Consequently, two main different regimes arise during the bubble generation process: the linear regime, at low gas flow rates, and the saturation regime, for larger gas flow rates. The existence of these two regimes was already confirmed and reported by the same authors in [12].

Figure 8 shows how f approaches its corresponding saturated value for the three different values

Table 4 Values of a_0 and f_{sat} obtained when fitting the experimental and numerical data by using Eq. 3

	Experiments		Simulations	
$U_{SL}[m/s]$	a_0 [m^{-1}]	f_{sat} [1/s]	a_0 [m^{-1}]	f_{sat} [1/s]
0.106	616.4	99.7	856.6	114.5
0.318	2033.9	228.4	2211.6	282.4
0.531	4483.6	376.3	6426.8	392.0

of U_{SL} in both experiments and simulations. The saturation frequency increases when increasing U_{SL}, which is a consequence of the corresponding increment of the liquid drag force, the main force in charged of detaching bubbles [25, 26]. Therefore, larger liquid drag forces are expected to produce smaller bubbles resulting in larger frequency values [11, 12]. This effect also explains why the linear slope at the origin, a_0, increases when increasing the liquid flow rate as observed for the three values of U_{SL} presented in the figures and in table 4.

As shown in figure 8, numerical simulations satisfactorily describe the behaviour of f observed in experiments. Numerical simulations agree qualitatively, but not quite quantitatively, with experimental results. They provide values in accordance with the experimental ones, but always larger (coherently, bubble sizes are expected to be slightly smaller, see section IV C). Differences in frequency between experimental and numerical results range from 3.5%, which would be within the margin of error of the mesh, to 34%, for the smallest value of U_{SG} and U_{SL}, which is a large difference, with an average value of 17%. As commented in Section III B 3, the boundary condition of the solid-air-water contact line is the key of this problem. A constant contact angle of 25^o is imposed on the vertical wall, corresponding to the one that best recreates the bubble detachment observed in the experiments. Nevertheless, the variation of the physical contact angle during the bubble formation process is not reproduced here, leading to CFD results always faster than the experimental ones. Future work should focus on the dynamic study of the contact angle, which is out of the scope of the study presented here.

A simple exponential fit is used with the values of bubble generation frequency in figure 8:

$$f = f_{sat}\left(1 - e^{\left(-\frac{a_0}{f_{sat}}U_{SG}\right)}\right) \tag{3}$$

Eq. 3 defines a simple function aiming to connect smoothly the linear part and the constant saturation value observed in figure 8, but it does not pretend to be a model for the bubble generation frequency. Only two parameters are considered in Eq. 3, the initial slope a_0 of the linear regime, and the value of the saturation frequency f_{sat}. According to the first-order Taylor series expansion of Eq. 3, f tends to $f_0 = a_0 U_{SG}$ when U_{SG} tends to zero. On the other hand, Eq. 3 tends to f_{sat} for larger values of U_{SG}. Both parameters have a clear physical meaning, as explained below. Assuming a regular generation of bubbles in size, the gas flow rate injected into the capillary must be equal to the bubble volume times the frequency, $Q_G = V_B f$, which leads to $f = Q_G/V_B = AU_{SG}/V_B$, in terms of the gas flow rate or the superficial gas velocity. Matching this expression with the first-order Taylor series expansion of Eq. 3 shows that $a_0 = A/V_B$. The initial slope of the linear regime corresponds to the maximum value of the ratio f/U_{SG} for each given U_{SL}. Then, a_0 is related to the minimum bubble volume that can be generated for each given U_{SL}, that is, $V_B|_{min} = A/a_0$. The saturation frequency is related in turn to the minimum time required to form a bubble, marking a limiting scale for the bubble generation process [11].

Table 4 summarises the values obtained for a_0 and f_{sat} when fitting both the experimental and numerical data by using Eq. 3. In every case, these values were found to be of the same order of magnitude for numerical and experimental values, but larger for the simulations.

B. Bubble velocity and void fraction

The bubble velocity is presented in figure 9 as a function of the average mixture superficial velocity U_M. It shows how, as expected, U_G increases when U_M increases and how both the experimental and the numerical data follow linear tendencies. The bubble velocity data fits the drift-flux model, defined by Zuber & Findlay [27], which under the hypothesis of negligible gravity levels or non-dominant gravitational forces can be written as [6, 28, 29]:

$$U_G = C_0 U_M = C_0(U_{SG} + U_{SL}), \tag{4}$$

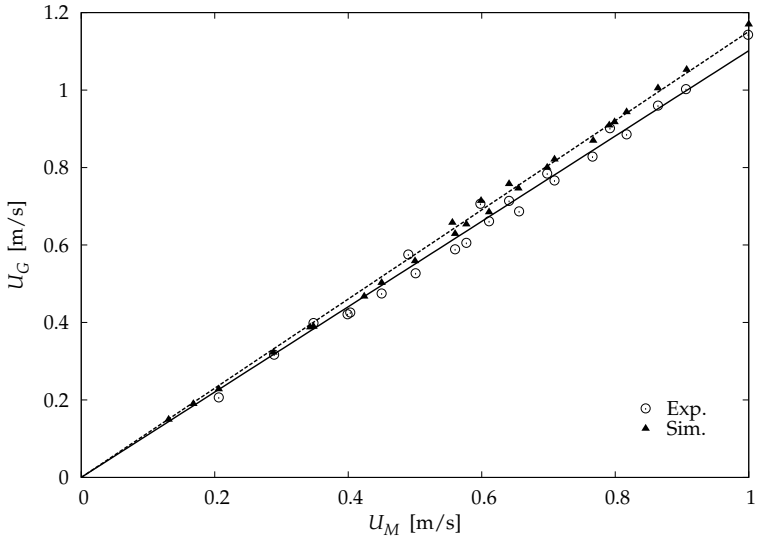

Fig. 9 Bubble velocity as a function of the mixture superficial velocity. *Empty symbols*: experimental data, *solid symbols*: numerical data. *Lines*: fitting of the data by using Eq. 4, with $C_0 = 1.10$ for experimental data (solid line) and $C_0 = 1.15$ for numerical simulation (dashed line)

where C_0 is the void fraction distribution coefficient, which considers both the effect of the non-uniform velocities of the gas and liquid phases and of the void profiles through the capillary diameter. Following Eq. 4, the value of C_0 has been calculated using a linear fitting in figure 9. A value of $C_0 = 1.10$ was found for the experimental data. Numerical simulations correctly reproduced the same behaviour than the one observed in the experiments, with $C_0 = 1.15$ (4.5% greater than in the experiments). In both cases, the value of C_0 is coherent with the range 1.1-1.2 reported in the related literature for similar two-phase flows [6, 29, 30].

Both values of C_0 (greater than 1) prove that bubbles move faster than the mixture, which is due to the fact that bubbles move mainly through the centreline of the capillary, not being attached to the upper part of the capillary in any case. It proves the negligible role of the gravitational forces [29], agreeing with the small Bond number value in the experiments, see section II, and validates the absence of gravity in the CFD simulations. The percentage of error with respect to the experimental data range from 0.8% to 19.3%, for the smallest value of U_{SG} and U_{SL}, with an average value of 5.4%.

Combining Eqs. 2 and 4, an analytical prediction of the volume void fraction as a function of

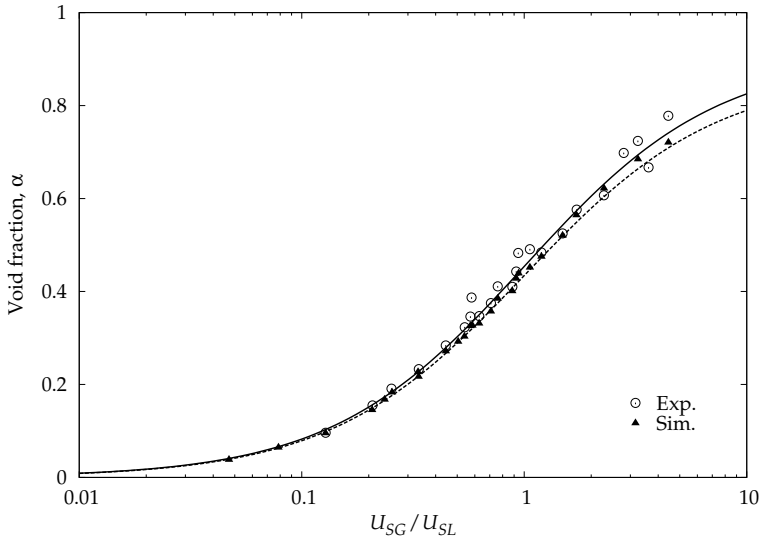

Fig. 10 Void fraction as a function of the ratio of the gas and liquid superficial velocities. *Empty symbols*: experimental data, *solid symbols*: numerical data. *Lines*: theoretical prediction given by Eq. 5, with $C_0 = 1.10$ for experimental data (solid line) and $C_0 = 1.15$ for numerical simulation (dashed line)

the gas and liquid superficial velocities can be found:

$$\alpha = \frac{1}{C_0 \left(1 + \frac{U_{SL}}{U_{SG}}\right)} \tag{5}$$

Figures 10 shows the volume void fraction as a function of the ratio between the gas and liquid superficial velocities. The prediction of α provided by Eq. 5 has also been plotted using the corresponding value of C_0. Both experimental and numerical data fit well to their respective prediction. The values of void fraction were found to be slightly smaller in the numerical simulations, coherently with their previously observed greater values of velocity. A minimum relative error of 0.8% was found with respect to the experimental data, being 15.5% the maximum relative error and 5.0% the average relative error. Two points appear below the value $U_{SG}/U_{SL} = 0.1$. As explained before, additional numerical simulations were run for very small values of U_{SG} (0.025 m/s). 3D numerical simulations proved thus to be useful in this case by providing information that was not available from the experiments.

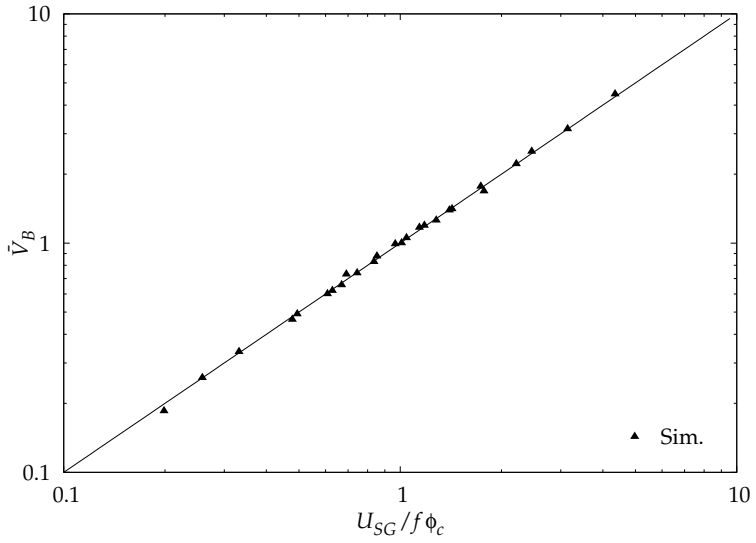

Fig. 11 Normalised bubble volume as a function of $U_{SG}/(f\phi_c)$. *Symbols*: simulation data. *Line*: theoretical prediction given by Eq. 6

C. Equivalent diameter and unit cell length

Normalising the expression $Q_G = V_B f$ with the cross-section area times the capillary diameter, a non-dimensional expression of the bubble volume can be obtained:

$$\bar{V}_B = \frac{U_{SG}}{f\phi_c}. \tag{6}$$

The bubble volume was measured from the 3D numerical simulations, see subsection III B 4. Since no direct measures of V_B could be performed in the experiments, Figure 11 shows the non-dimensional bubble volume as a function of the ratio $U_{SG}/(f\phi_c)$ for numerical data only. It shows how, as expected, the bubble volume increases when increasing the gas superficial velocity. Data fit well to the prediction of Eq. 6, which confirms that bubbles were generated with high regularity.

In order to provide a bubble size quantitative comparison between experiments and simulations, an equivalent diameter ϕ_B has been considered for each bubble. This equivalent diameter is estimated by matching the bubble volume predicted by Eq. 6 to the volume of a sphere with a diameter equal to ϕ_B. Being $V_S = \pi\phi_B^3/6$ the volume of such a sphere, the dimensionless volume of the sphere is $\bar{V}_S = 2\bar{\phi}_B^3/3$, where the bubble volume is again normalised with the cross-section area times the capillary diameter. The equivalent diameter, normalised with the capillary diameter, is

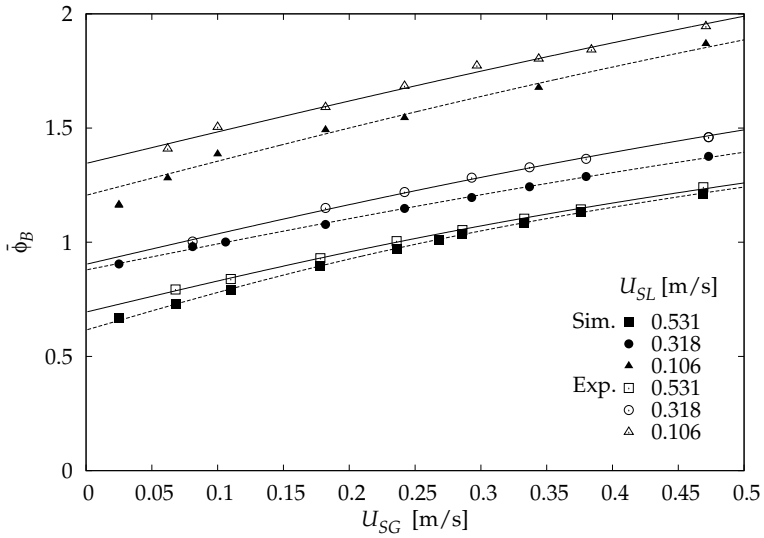

Fig. 12 Normalised equivalent diameter $\bar{\phi}_B$ as a function of the gas superficial velocity U_{SG}. *Empty symbols*: experimental data, *solid symbols*: numerical data. *Lines*: solid and dashed lines, given by Eq. 7, correspond to experimental and numerical data, respectively

then computed as the result of matching $\bar{V}_B$ and $\bar{V}_S$:

$$\bar{\phi}_B = \left(\frac{3}{2} \frac{U_{SG}}{f \phi_c} \right)^{1/3} \tag{7}$$

Figure 12 shows the dimensionless equivalent diameter as a function of the gas superficial velocity. Differences in equivalent diameter between experimental and numerical results range from 1.1% to 9.1% with an average of 5.2%. The equivalent diameter is estimated using Eq. 7 in both cases. The lines correspond to Eq. 7, in which the fitting of f provided by Eq. 3 is used. Both experimental and numerical data correctly agree with the combination of Eqs. 3 and 7. As a consequence of the faster bubble generation process observed in the numerical simulations, the equivalent diameters are found to be slightly smaller in numerical simulations than those from experiments, especially at low liquid superficial velocity. It can also be observed that increasing the liquid superficial velocity causes the bubble volume and thus the equivalent diameter to decrease. Finally, figure 12 allows distinguishing the bubble and the slug flow regime by means of the Dukler's criterion, see section IV. Bubbles with $\bar{\phi}_B < 1$ correspond to the bubble flow regime, whereas these with $\bar{\phi}_B > 1$ fall into the category of the slug flow.

The last part of the validation of the numerical simulations focuses on the unit cell length, L_{UC}. Bubbles displace at a speed of U_G, being $1/f$ the time required to form and detach a single bubble (same time as the one required to generate a new unit cell). As a consequence, the unit cell length must be equal to the bubble velocity times the time required to form a unit cell. The unit cell length can then be expressed as:

$$\bar{L}_{UC} = \frac{U_G}{f\phi_c}, \tag{8}$$

where it is normalised with the capillary diameter. Values of the non-dimensional unit cell length are plotted in figure 13. Both data, corresponding to experimental and numerical data, fit well to the prediction of Eq. 8. Relative errors range from 2.0% to 20.8% with an average value of 9.5%.

Figure 14 plots the dimensionless unit cell length $\bar{L}_{UC}$ as a function of the gas superficial velocity U_{SG} for each liquid superficial velocity. A theoretical prediction can be found in this case when using Eq. 4 into Eq. 8:

$$\bar{L}_{UC} = \frac{C_0(U_{SG} + U_{SL})}{f\phi_c} \tag{9}$$

Figure 14 shows a non-monotonic behaviour with a minimum value of $\bar{L}_{UC}$ for each given value of U_{SL}. This minimum is located at the crossover region between the linear and the saturation regime and it can be explained taking into account the dependence of f in U_{SG}. The time required to form a single bubble decreases as the bubble generation frequency increases, which in turn decreases the total quantity of liquid that can be injected into the unit cell, producing shorter unit cells. Within the linear regime, small variations of the gas superficial velocity typically cause the generation frequency to largely increase, which decreases rapidly the unit cell length towards its minimum value. On the other hand, within the saturation regime, the increase of the gas superficial velocity makes the bubbles grow in size while maintaining almost the same frequency. This enlargement of bubbles explains the smooth increasing of the unit cell length beyond its minimum value, as U_{SG} increases. As previously discussed, since the bubble formation process is found to be faster in

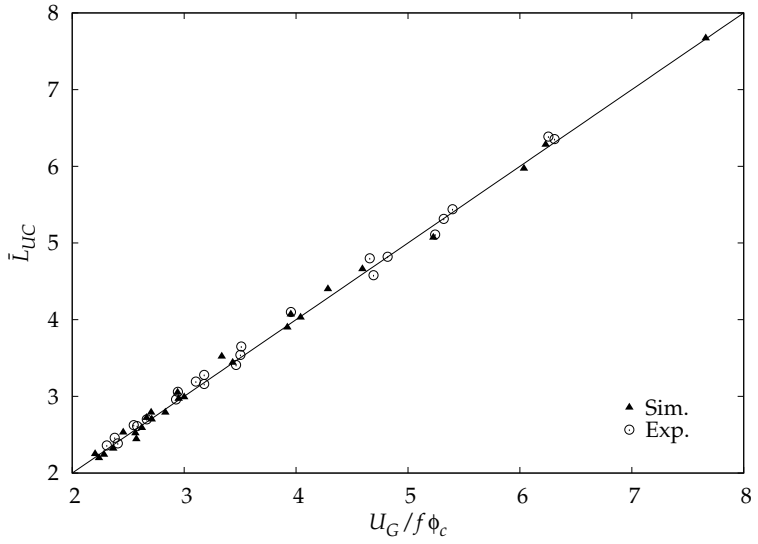

Fig. 13 Normalised unit cell length as a function of $U_G/f\phi_c$. *Empty symbols*: experimental data, *solid symbols*: numerical data. *Line*: theoretical prediction given by Eq. 8

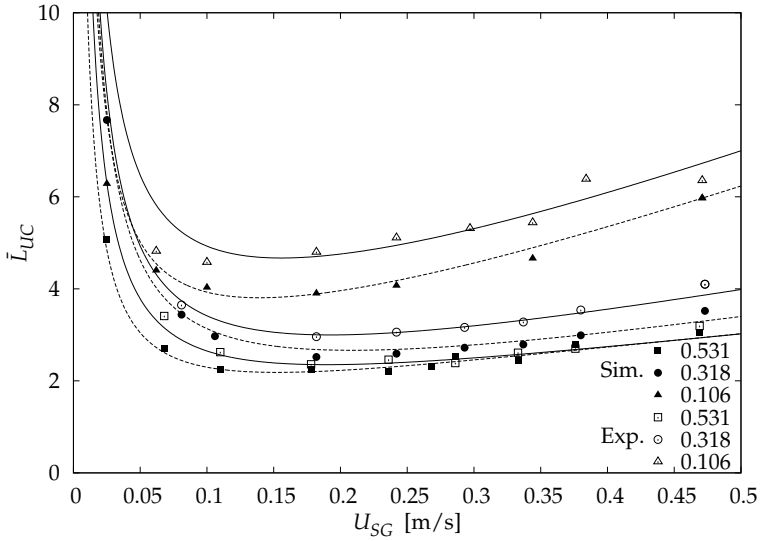

Fig. 14 Normalised unit cell length as a function of the gas superficial velocity. *Symbols*: experimental and numerical data. *Lines*: solid and dashed lines, given by Eq. 9, correspond to experimental and numerical data, respectively

numerical simulations, smaller unit cell lengths than in experiments are obtained.

V. Conclusions

This paper presents a study on the numerical simulation of bubbles generated in a 3D T-junction (1 mm internal diameter capillaries), with an air/water mixture, using the commercial

CFD solver ANSYS Fluent v15.0.7. Numerical results were compared with experimental data, both cases following the same conditions.

Several trains of bubbles were simulated with high regularity and small dispersion in size during the bubble formation process. No artificial pinch-off mechanism was required for the detachment of bubbles. Bubble or slug flow regimes were obtained in all cases, both in experiments and numerical simulations. Regarding the slug flow, only short and middle Taylor bubbles were generated. Numerical simulations satisfactorily reproduced the formation of bubbles, both in the stabilised shape and in the evolution of shape during the formation of bubbles.

Several parameters were compared between 3D-CFD results and experimental data, such as bubble generation frequency, bubble velocity, void fraction, bubble equivalent diameter and unit cell length. Results were found to be of the same order of magnitude in both simulations and experiments, though due to a constant contact angle being imposed on the vertical wall, CFD simulations always predicted larger frequencies, resulting in smaller sized bubbles. Future work should focus in studying into more details the boundary condition of the solid-air-water contact line in the numerical simulation, in order to further improve these results. 3D-CFD simulations allowed to study new zones of interest (especially at low gas flow rate) and new parameters such as the bubble volume (not available from experimental results), showing that this is a useful tool to improve our current experimental knowledge on two-phase flows in minichannels.

Acknowledgments

This work has been financially supported by the Spanish *Ministerio de Economía y Competitividad, Secretaría de Estado de Investigación, Desarrollo e Innovación* (Project numbers AYA2012-34131 and MTM2013-46313-R) and the *Generalitat de Catalunya* (Grant number 2014-SGR-1471).

References

[1] Yamamotoa, K. & Ogata, S., "Effects of T-junction size on bubble generation and flow instability for two-phase flows in circular microchannels," *Int. J. Multiphase Flow* **49**, 2013, pp. 24-30.

[2] Yamamotoa, K. & Ogata, S., "Drag reduction of slug flows in microchannels by modifying the size of T-junctions," *Int. J. Multiphase Flow* **62**, 2014, pp. 67-72.

[3] Qian, D. & Lawal, A., "Numerical study on gas and liquid slugs for Taylor flow in a Tjunction microchannel," *Chem Eng Sci* **61(23)**, 2006, pp. 7609-7625.

[4] Kashid, M. N., Platte, F., Agar, D. W. & Turk, S., "Computational modelling of slug flow in a capillary microreactor," *J Comput Appl Math* **203(2)**, 2007, pp. 487-497.

[5] D Menech, M., Garstecki, P., Jousse, F. & Stone, H. A., "Transition from squeezing to dripping in a microfluidic T-shaped junction," *J Fluid Mech* **595**, 2008, pp. 141-161.

[6] Arias, S., Legendre, D. & González-Cinca, R., "Numerical simulation of bubble generation in a T-junction," *Computers & Fluids* **56**, 2012, pp. 49-60.

[7] Ngo, I. L., Dang, T. D., Byon, C. & Joo, S. W., "A numerical study on the dynamics of droplet formation in a microfluidic double T-junction," *Biomicrofluidics* **9**, 2015, pp. 024107.

[8] Malekzadeh, S. & Roohi, E., "Investigation of Different Droplet Formation Regimes in a T-junction Microchannel Using the VOF Technique in OpenFOAM," *Microgravity Sci. Technol.* **27**, 2015, pp. 231-243.

[9] Shi, Y., Tang, G. H. & Xia, H. H., "Lattice Boltzmann simulation of droplet formation in T-junction and flow focusing devices," *Computers & Fluids* **90**, 2014, pp. 155-163.

[10] Ben Saad, S., Gentric, C., Fourmigue, J. F., Clement, P. & Leclerc, J. P., "CFD and experimental investigation of the gas-liquid flow in the distributor of a compact heat exchanger," *Chemical Engineering Research* & Design **92(11)**, 2014, pp. 2361-2370.

[11] Arias, S., Ruiz, X., Ramírez-Piscina, L., Casademunt, J. & González-Cinca, R., "Experimental study of a microchannel bubble injector for microgravity applications," *Microgravity Sci. Technol.* 21, 2009, pp. 107-111.

[12] Arias, S., González-Cinca, R., Ruiz, X., Ramírez-Piscina, L. & Casademunt, J., "Characterization of the performance of a minibubble generator in conditions relevant to microgravity," *Colloids and Surfaces A: Physicochem. Eng. Aspects* **365**, 2010, pp. 52-55.

[13] Suo, M. & Griffith, P., "Two-phase flow in capillary tubes," *J. Basic Eng.* **86**, 1964, pp. 576-582.

[14] Rezkallah, K. S., "Weber number based flow-pattern maps for liquid-gas flows at microgravity," *Int. J. Multiphase Flow* **22(6)**, 1996, pp. 1265-1270.

[15] ANSYS Academic Research, Release 15.0,7, Help System, ANSYS, Inc, 2014.

[16] Youngs, D. L., "Time-Dependent Multi-Material Flow with Large Fluid Distortion," K. W. Morton and M. J. Baines, editors, Numerical Methods for Fluid Dynamics. Academic Press, 1982.

[17] Brackbill, J. U., Kothe, D. B. & Zemach, C., "A Continuum Method for Modeling Surface Tension," *J. Comput. Phys.* **100**, 1992, pp. 335-354.

[18] Huh, C. & Scriven, L.E., "Hydrodynamic model of steady movement of a solid/liquid/fluid contact line," *J. of Colloid and Interface Science* **35(1)**, 1971, pp. 85-101.

[19] Afkhami, S., Zaleski, S. & Bussmann M., "A mesh-dependent model for applying dynamic contact angles to VOF simulations," *J. Comput. Phys.* **228**, 2009, pp. 5370-5389.

[20] Garstecki, P., Fuerstman, M.J., Stone, H.A., & Whitesides, G.M., "Formation of droplets and bubbles in a microfluidic T-junction-scaling and mechanism of break-up," *Lab on a Chip* **6**, 2006, pp. 437-446.

[21] Oishi, M., Kinoshita, H., & Oshima, M., "Investigation of micro droplet formation in a T-shaped junction using multicolor confocal micro PIV," *1st ASME Micro/Nanoscale Heat Transf. Int. Conf., Amer. Soc. Mech. Eng.*, 2008, pp. 297-301.

[22] Colin, C. & Fabre, J., "Gas-liquid pipe flow under microgravity conditions: influence of tube diameter on flow pattern and pressure drops," *J. Adv. Space Research* **16**, 1995, pp. 137-142.

[23] Dukler, A. E., Fabre, J. A., McQuillen, J. B. & Vernon, R., "Gas-liquid flow at microgravity conditions: flow patterns and their transitions," *Int. J. Multiphase Flow* **14**, 1988, pp. 389-400.

[24] Puccetti, G., Tosi, M., Pulvirenti, B. & Morini, G. L., "Flow patterns of an air-water mixture at the exit of a micro T-junction," *Experimental Thermal and Fluid Science* **67**, 2015, pp. 62-69.

[25] Carrera, J., Ruiz, X., Ramírez-Piscina, L., Casademunt, J. & Dreyer, M., "Generation of a monodisperse microbubble jet in microgravity," *AIAA Journal* **46(8)**, 2008, pp. 2010-2019.

[26] Fu, T., Ma, Y., Funfschilling, D., Zhu, C. & Li, H. Z., "Squeezing-to-dripping transition for bubble formation in a microfluidic T-junction," *Chem Eng Sci* **65(12)**, 2010, pp.3739-3748.

[27] Zuber, N. & Findlay, J., "Average Volumetric Concentration in Two-Phase Systems," *Trans ASME Jul Ht Transfer* **87**, 1969, pp. 453-468.

[28] Colin, C., Fabre, J. & Dukler, A. E., "Gas-liquid flow at microgravity conditions - I Dispersed bubble and slug flow," *Int. J. Multiphase Flow* **17**, 1991, pp. 533-544.

[29] McQuillen , J., Colin, C. & Fabre J., "Ground-based gas-liquid flow research in microgravity conditions: state of knowledge," *Space Forums* **3**, 1998, pp. 165-203.

[30] Bendiksen, K. H., "An experimental investigation of the motion of long bubbles in inclined," *Int. J. Multiphase Flow* **10**, 1984, pp. 467-483.